Journal of Power Sources 195 (2010) 3814–3821

Contents lists available at ScienceDirect

Journal of Power Sources

journal homepage: www.elsevier.com/locate/jpowsour

Corrosion properties and contact resistance of TiN, TiAlN and CrN coatings in simulated proton exchange membrane fuel cell environments

L. Wang[a], D.O. Northwood[a], X. Nie[a,*], J. Housden[b], E. Spain[b], A. Leyland[c], A. Matthews[c]

[a] Department of Mechanical, Automotive, and Materials Engineering, University of Windsor, 401 Sunset Avenue, Windsor, ON, Canada N9B 3P4
[b] Tecvac Ltd., Buckingway Business Park, Swavesey, Cambridge, CB24 4UG, UK
[c] Department of Engineering Materials, University of Sheffield, Sheffield, S1 3JD, UK

ARTICLE INFO

Article history:
Received 4 December 2009
Received in revised form
23 December 2009
Accepted 29 December 2009
Available online 14 January 2010

Keywords:
PEM fuel cell
Metallic bipolar plate
PVD coating
Contact resistance
Corrosion resistance

ABSTRACT

In this study, the contact resistance (CR) and electrochemical properties of TiN, CrN and TiAlN electron beam physical vapor deposition (EBPVD) coatings and their stainless steel 316L (SS316L) substrate were investigated in a simulated proton exchange membrane (PEM) fuel cell environment. The potentiodynamic polarization corrosion tests were conducted at 70 °C in 1 M H_2SO_4 purged with either O_2 or H_2, and the potentiostatic corrosion tests were performed under both simulated cathodic (+0.6 V vs. Ag/AgCl reference electrode purged with O_2) and anodic conditions (−0.1 V vs. Ag/AgCl reference electrode purged with H_2) for a long period (4 h). SEM was used to observe the surface morphologies of the samples after corrosion testing. All the TiN-, TiAlN- and CrN-coated SS316L showed a lower CR than the uncoated SS316L. While the corrosion performance of the coatings was dependent on the cathodic and anodic conditions, the CrN coating exhibited a higher (in the anodic environment) or similar (in the cathodic environment) corrosion resistance to the uncoated SS316L. Thus, the CrN-coated SS316L could potentially be used as a bipolar plate material in the PEM fuel cell environment. Although the EBPVD process greatly reduced number of pinholes in the coatings compared to other plasma enhanced reactive evaporations, future research efforts should be directed to eliminate the pinholes in the coatings for long-term durability in fuel cell applications.

1. Introduction

The proton exchange membrane fuel cell (PEMFC) is gaining worldwide interest [1–11] due to its advantages over other fuel cells such as delivering high power density, a low weight and volume. Moreover, PEM fuel cells operate at relatively low temperatures (<100 °C), resulting in a better durability of system components. To date, the major challenges for the commercial application of PEMFC systems include reducing the cost and weight of the fuel cell stack. One of the key components of the fuel cell stack is the bipolar plate which has the main functions of distributing and separating the cathodic and anodic reactant gases, and collecting and transmitting electric current. In terms of weight, volume and cost, bipolar plates are one of the most significant parts of a fuel cell stack [5,8,12]. Thus, to meet the PEMFC cost targets, as well as meeting the fundamental required characteristics such as high electrical conductivity, and mechanical and chemical stability, the bipolar plate materials are expected to also be inexpensive, lightweight and easily manufactured.

Graphite composites have been considered the standard material for PEMFC bipolar plates because of their low surface contact resistance and high corrosion resistance. Unfortunately, graphite and graphite composites are brittle and have poor cost effectiveness for high volume manufacturing processes. Metallic bipolar plate materials such as aluminum, stainless steel, titanium, and nickel have been considered as possible alternative materials which have good electrical conductivity, low material cost, versatile manufacturing processes and high mechanical strength [3,5,6,8,9,13–15]. Stainless steels are widely accepted as one of the leading PEMFC bipolar plate material candidates [8,9,14–16]. However, the main issue with metals is the degradation of the PEMFC caused by corrosion of the bipolar plates leading to an increase in the interfacial contact resistance (ICR) between the bipolar plates and the gas diffusion layer (GDL). Also, the metal ions produced by corrosion, will migrate to the Nafion® membrane and displace H^+ ions in the membrane, thereby, reducing the conductivity of the membrane and the overall efficiency of the fuel cell [15]. Thus, metallic plates with protective coatings have been extensively studied to impart the stainless steel bipolar plates with sufficient corrosion resistance and contact conductivity without increasing the cost to the level of that of noble metals [8,10,11,17–22].

* Corresponding author. Tel.: +1 519 253 3000x4148; fax: +1 519 973 7007.
E-mail address: xnie@uwindsor.ca (X. Nie).

0378-7753/$ – see front matter © 2010 Elsevier B.V. All rights reserved.
doi:10.1016/j.jpowsour.2009.12.127

Physical vapor deposition (PVD) hard ceramic coatings are widely applied as protective coatings in the fields of wear and corrosion protection. Titanium nitride (TiN) based and chromium nitride (CrN) based coatings are commonly used protective coatings for industrial applications [23–29]. Stainless steel bipolar plates coated using PVD methods have attracted much interest recently [18–21,30–32]. However, most of these studies were concentrated on TiN and DLC coatings. Further studies on the potential application of other ceramic hard coatings were needed, for example, CrN and TiAlN coatings which have been reported to have improved corrosion protection properties in salt solutions (3.5%) compared to TiN coatings [25,33]. The performance of TiAlN in a solid oxide fuel cell (SOFC) environment has been studied and concluded that TiAlN coatings were good candidates for SOFC interconnect applications at 700 °C [34]. However, few reports have been presented on the possibility of the coating used for PEM fuel cells.

In this study, the contact resistance (CR) and electrochemical properties of TiN-, CrN- and TiAlN-coated stainless steel 316L (SS316L) deposited using PVD technology have been determined in a simulated PEM fuel cell environment. The uncoated stainless steel 316L (SS316L) substrate was used as a reference material.

2. Experimental details

2.1. Test specimen preparation

TiN and CrN coatings were deposited using a single electron beam PAPVD system (Tecvac IP70L) [25,30,31]. The TiAlN coating was deposited using a twin electron beam PAPVD system (Tecvac IP35L) [23]. The coating chemical compositions were determined using glow discharge optical emission spectroscopy (GDOES). The GDOES used a 1000 RF Jovin-Yvon spectrometer, equipped with a 35-channel hemispherical monochromator. The chemical compositions of TiN, CrN and TiAlN were Ti:N = 50:50, Cr:N = 70:30 and Ti:Al:N = 35:15:50, respectively [35]. These coatings were deposited on mirror polished (Ra < 0.1 μm) AISI 316L stainless steel discs of 30 mm in diameter and 3 mm in thickness. Uncoated AISI 316L stainless steel discs were also polished and cleaned for use as a reference material.

2.2. Coating mechanical properties and structural characterization

Coating thicknesses were measured by a cross-sectional scanning electron microscope (SEM) observation. The crystalline structure of the coatings was analyzed by X-ray diffraction (XRD) which was performed on a Rigaku D/max 1200 X-ray diffractometer in a θ–2θ scan mode using CuKα radiation (30 kV, 30 mA). Samples were scanned from 10 to 100° in 2θ, and the scanning step was 0.02° in 2θ. A Hysitron Ub1 nanomechanical test system was employed to measure hardness and reduced elastic modulus (E_r) of the coated discs at a normal load of 4 mN using the Oliver and Pharr analysis method [36]. The indenter used was a three-sided pyramid Berkovich diamond with a tip radius of curvature of ~100 nm.

2.3. Contact resistance (CR)

The CR measurements were conducted on all coated and uncoated stainless steel samples. The CR measurement method used in this study was similar to that reported by Wang et al. [9]. In this setup (Fig. 1), two pieces of conductive carbon paper (Electrochem Inc.) were sandwiched between the steel sample and two copper plates. A GOM-802 DC Mill–Ohm Omega meter was used in a 4-wire measurement mode to measure the total resistance drop through this setup with the increase in compaction force. The compaction force was applied using a manual test stand (Rima Spring tester). Before each measurement, the copper plates were polished to remove the natural oxide film using # 1200 ANSI grit SiC abrasive paper. The carbon paper was only used once for each measurement test. The maximum compaction pressure applied in the CR test is 300 N cm^{-2} (3 MPa). With this approach, the measured resistance (R_{totl}) consists of (a) the bulk resistance of two flat carbon papers, $2R_{cp}$; (b) the bulk resistance of specimen (stainless steel substrate (R_{ss}) with/without PVD coatings (R_{film})), $R_s = R_{ss} + (2R_{film})$; (c) two interfacial contact resistances between flat carbon paper and test specimen, $2R_{cp/Rs}$; (d) two interfacial contact resistances between copper plate and flat carbon plate, $2R_{Cu/cp}$. Thus, the measured resistance can be expressed as $R_{totl} = 2R_{cp} + R_{ss} + (2R_{film}) + 2R_{cp/Rs} + 2R_{Cu/cp}$. Since the resistance of carbon paper (R_{cp}) and stainless steel substrate (R_{ss}) is very small (compared with the other resistances) and therefore negligible, the measured resistance can be expressed as $R_{totl} \approx 2R_{film} + 2R_{cp/Rs} + 2R_{Cu/cp}$. The interfacial contact resistance between carbon paper and copper plates ($2R_{Cu/cp}$) can be gained by a calibration in which only one layer of carbon paper was sandwiched between two copper plates. By deducting the $R_{Cu/cp}$, the contact resistance ($R_C = (R_{totl} - 2R_{Cu/cp})/2$) consisting of interfacial contact resistance between carbon paper and test specimens ($R_{cp/Rs}$) and electrical resistance of coatings (R_{film}) can be obtained, i.e., $R_C = R_{film} + R_{cp/Rs}$.

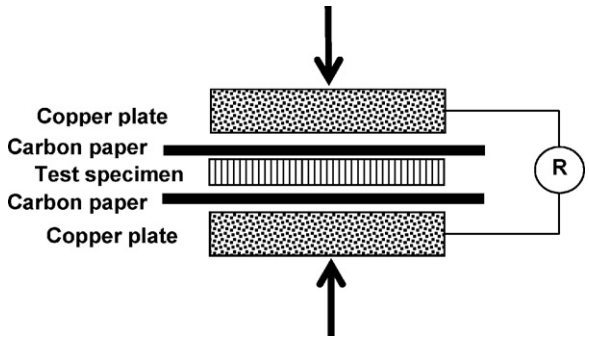

Fig. 1. Schematic of the contact resistance test setup.

2.4. Corrosion properties

The corrosion properties of uncoated and coated samples were characterized by two electrochemical methods, namely potentiodynamic and potentiostatic polarization tests. The tests were conducted in a three-electrode system test unit with a platinum counter electrode of 1 cm^2 and an Ag/AgCl, 3 M KCl electrode as the reference electrode using a SP-150 Potentiostat (Biologic Science Instruments) controlled by a computer. To simulate the aggressive PEMFC environment, all the electrochemical characterizations were performed in a 1 M sulphuric acid solution at 70 °C with H_2 or O_2 purging to simulate the anodic and cathodic environments, respectively.

In the potentiodynamic tests, the initial potential was −0.1 V vs. open circuit potential (OCP), and the final potential was 1.2 V vs. Ag/AgCl electrode. The scan rate was 1 mV s^{-1}. The calculated polarization resistance (R_p) gained from the potentiodynamic polarization tests were used to evaluate the corrosion protection characteristic since R_p is inversely proportional to the instantaneous interfacial reaction rates, i.e., corrosion rates.

The current density change under the simulated application potentials in the simulated PEM fuel cell environments during a period of time was monitored by the potentiostatic polarization technique. By this monitoring, the corrosion behaviors of samples during the period of time under the simulated application conditions can be observed since the current density is

Table 1
Coating thickness, hardness and reduced elastic modulus.

	Thickness (μm)	Hardness (H/GPa)	Reduced elastic modulus (E_r/GPa)
TiN	2.0 ± 0.2	25.5 ± 0.5	355.06 ± 30.5
CrN	2.0 ± 0.1	24.8 ± 1.0	283.17 ± 5.1
TiAlN	1.9 ± 0.05	26.3 ± 3.0	294.39 ± 5.2

proportional to corrosion rate. The potentiostatic polarization tests were conducted for 4 h at the anodic and cathodic conditions: the applied potential was −0.1 V vs. Ag/AgCl electrode with H_2 purging (anodic) and +0.6 V vs. Ag/AgCl electrode with O_2 purging (cathodic). The surface morphologies of samples after corrosion testing were observed using SEM with energy dispersive X-ray analysis (EDX).

3. Results and discussion

3.1. Coating mechanical properties and structural characterization

Fig. 2 shows the cross-sectional SEM micrographs of the TiN, CrN and TiAlN coatings. All the coatings showed a dense microstructure with a well-defined coating/substrate interface and had a similar thickness of about 2 μm. Table 1 summarizes the measured coating thickness, hardness and reduced elastic modulus for TiN, CrN and TiAlN coatings on the SS316L substrate. The TiAlN coating exhibits a somewhat higher hardness of 26.3 GPa than the TiN (25.5 GPa) and CrN (24.8 GPa) coatings. TiN has the highest reduced elastic modulus, ~355 GPa, while CrN and TiAlN coatings have a similar reduced elastic modulus, about ~290 GPa.

Fig. 3 shows the XRD patterns of the coatings. In the XRD pattern of the TiN coating (Fig. 3(a)), the main diffraction peaks are (1 1 1), (2 0 0), (3 1 1) and (2 2 2). In the TiAlN coating (Fig. 3(a)), the major diffraction peaks of (1 1 1) and (2 0 0) remain. With the introduction of Al into the TiN structure, the intensity of the (3 1 1) and (2 2 2) diffraction peaks declines. The XRD patterns show that both the TiN and TiAlN coatings have a cubic TiN (B1 NaCl) structure and no hexagonal AlN (B4 wurtzite) structure. The CrN coating (Fig. 3(b)) has an orthorhombic crystal structure, of which (1 1 0), (1 0 1), (0 2 0) and (1 3 0) are the major CrN diffraction peaks, and a β-Cr_2N phase (inset in Fig. 3(b)).

3.2. Contact resistance (CR)

The contact resistance (R_C) results are shown in Fig. 4. The inset in Fig. 4 is an expanded plot at compacting pressures in the range 200–300 N cm^{-2}. With increasing compaction pressure, the resistance of the materials decreases rapidly at a low compaction pressure range (<70 N cm^{-2}) and then decreases gradually at higher compaction pressures. At a given compaction pressure, the resistance increases in the order of TiAlN < CrN < TiN < SS316L. For example, at a compaction pressure of 274.4 N cm^{-2}, the contact resistance of TiAlN, CrN, TiN and uncoated SS316L are 7.5, 21.8, 35.0 and 66.4 mΩ cm^2, respectively. The uncoated stainless steel sample has a higher contact resistance than the coated samples, which can be attributed to the natural oxide passive layer on the steel surface. The contact resistance of CrN coating appears to be lower than that of the TiN coating, and the TiAlN coating shows the lowest value in contact resistance. According to the band structure, strongly hybridized N 2p and Ti 3d orbitals contribute nine valence electrons to the electrical conductivity of TiN [37]. The Al atoms introduced into the TiN structure should generally give a polar interphase resulting in metallic bonding between Ti–Al or covalent bonding (Ti–N and Al–N) [38] and, therefore, lead to an increase in the electrical conductivity of the TiAlN coating compared to the TiN coating. It has been reported that the electrical resistance of TiN and TiAlN coatings are significantly affected by the phase structure, N content and the defect density in the coatings [37–39]. For instance, since AlN is a good electrical insulator, the electrical conductivity of a TiAlN coating should be significantly decreased if the hexagonal AlN (B4 wurtzite) structure is present in a TiAlN coating. However, there was no AlN phase formed in the TiAlN coating deposited in this study. The low contact resistance of the CrN coating was due to the composition (i.e., 30% N) of the coating and the presence of two Cr nitride phases (i.e., CrN and Cr_2N)

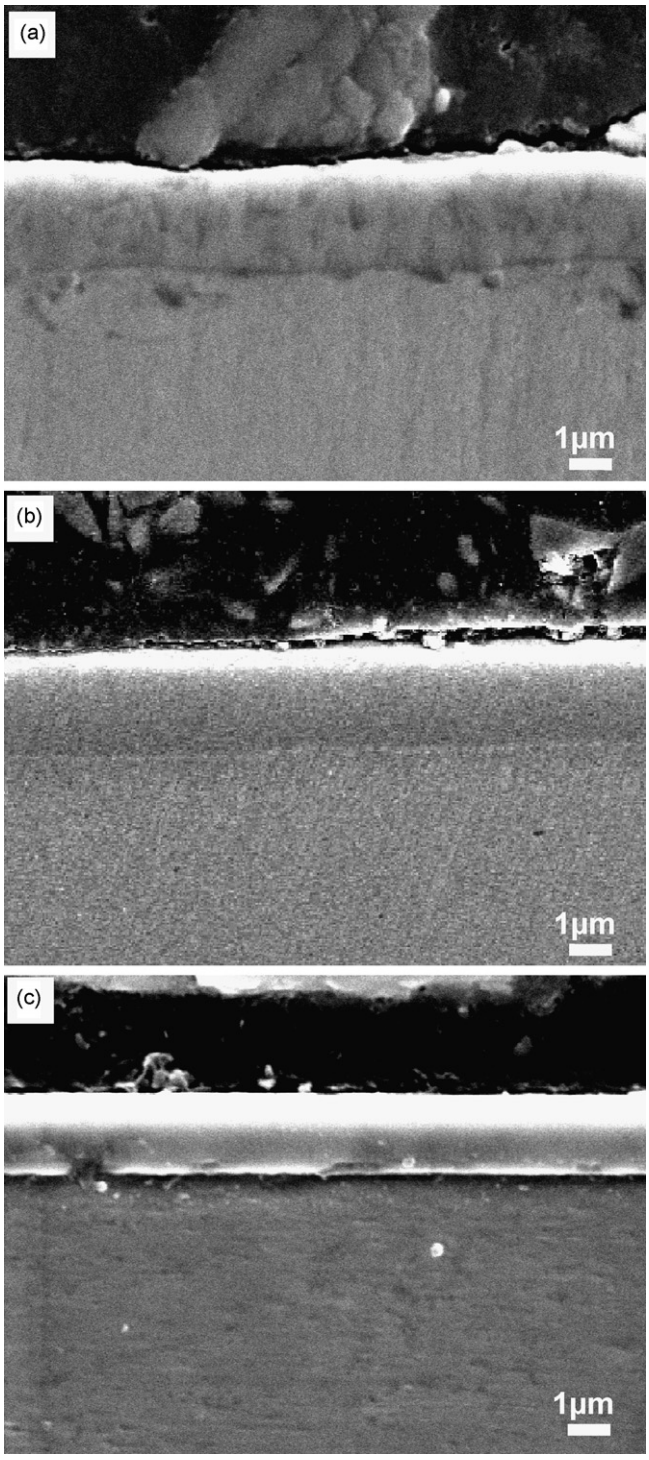

Fig. 2. Cross-sectional SEM micrographs of (a) TiN, (b) CrN and (c) TiAlN coatings.

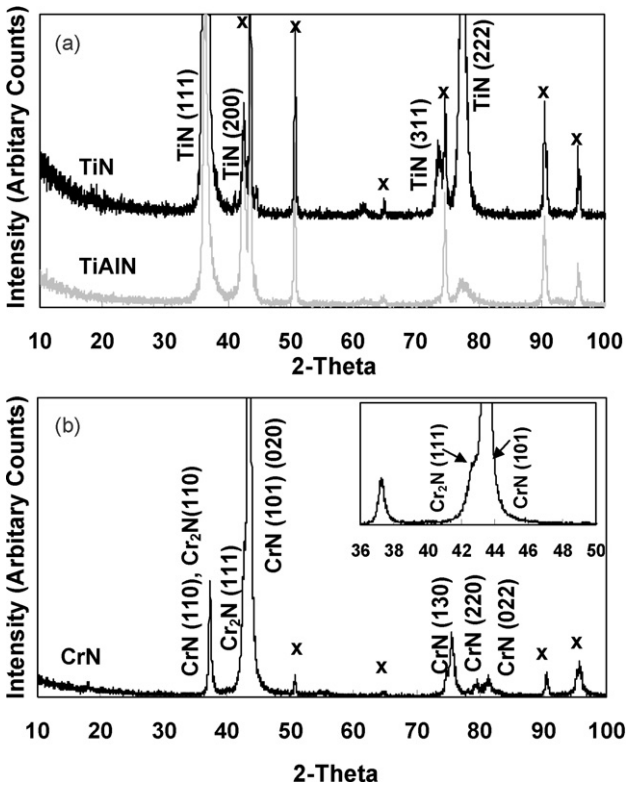

Fig. 3. XRD patterns of coatings (a) TiN, TiAlN and (b) CrN. The peaks labelled "×" originate from the 316L stainless steel substrate.

as shown in the XRD pattern of Fig. 3(b). A Cr_2N phase is usually electrically conductive. The CrN phase in this paper likely was a substoichiometric CrN_x ($x < 1$) phase which is often reported to be metallic-like [40]. A low CR value of CrN/Cr_2N layer formed on Ni–Cr base and Fe-base stainless steel alloys by thermal (gas) nitridation has also been reported by Brady and co-workers [41–43].

3.3. Potentiodynamic polarization behavior

Fig. 5 shows the potentiodynamic polarization curves for TiN-, CrN-, TiAlN-coated, and uncoated SS316L specimens in the simulated anodic and cathodic environments, i.e., with H_2 purging (Fig. 5(a)) and O_2 purging (Fig. 5(b)). The corrosion potential (E_{corr}), current density (i_{corr}) and polarization resistance (R_p) obtained by Tafel calculations for uncoated and coated SS316L are given

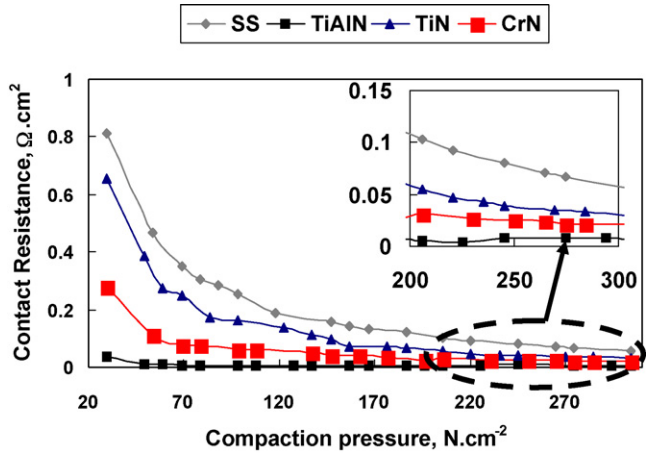

Fig. 4. Contact resistances for the coated and uncoated stainless steel samples.

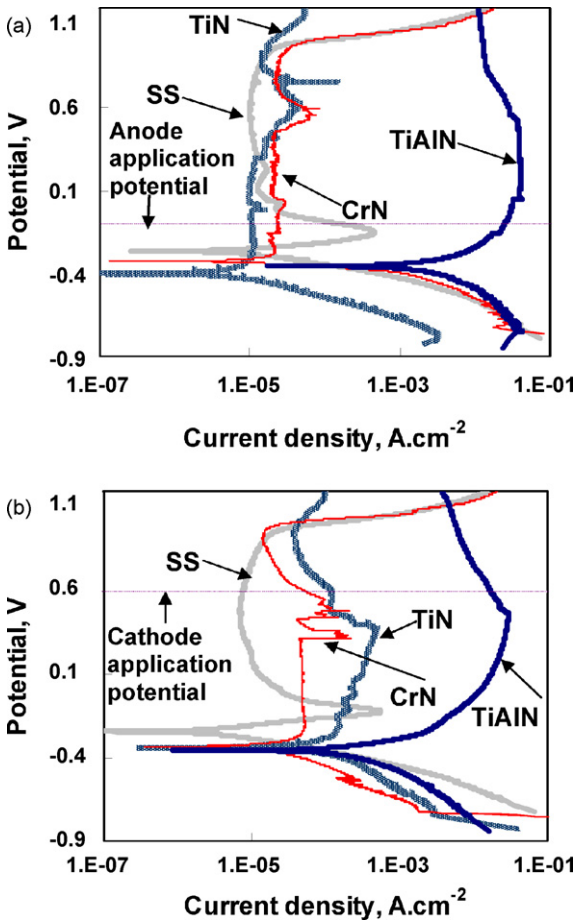

Fig. 5. Potentiodynamic polarization curves for TiN-, CrN-, TiAlN-coated and uncoated stainless steel 316L samples in a 1 M sulphuric acid solution at 70 °C with (a) H_2 purging and (b) O_2 purging.

in Table 2. The corrosion resistances in anodic (H_2 bubbled) and cathodic (O_2 bubbled) environments increase in the order of TiAlN < SS316L < CrN < TiN and TiAlN < TiN < CrN < SS316L, respectively. The SS316L substrate shows a typical polarization curve of passive metals in either H_2 or O_2 (Fig. 5(a and b)) bubbled environments with active, passive and transpassive regions. The corrosion potential (E_{corr}) in O_2 bubbled environment (−0.24 V) is higher than that of in H_2 bubbled environment (−0.27 V) and corrosion current density is about 7 times lower in O_2 bubbled environment than the H_2 bubbled one. This is not unexpected, because stainless steel is more readily passivated in an O_2-containing environment and the passive layer formed is more stable and thicker than in a H_2-containing environment [16]. For the TiN-coated sample, the corrosion potential is higher in an O_2 bubbled environment (−0.34 V) than in a H_2 bubbled environment (−0.38 V) but the corrosion current density is higher in the O_2 environment. The polarization resistance of TiN is 20 times higher in a H_2-purged environment than in O_2-purged environment. The effect of gas purging is not significant for the CrN coating and the corrosion current density and corrosion potential are similar in both environments. The TiAlN-coated material has a similar corrosion potential in either a H_2 or an O_2 environment but a higher corrosion current density in a H_2 environment than in an O_2 environment (Table 2). For the CrN and TiAlN coatings, the polarization corrosion resistances in the simulated cathodic environment are 2 and 11 times higher than those in an anodic environment.

From the potentiodynamic polarization curves (Fig. 5), at the anode application potential (E_{ap}), i.e., −0.1 V vs. Ag/AgCl electrode,

Table 2
Potentiodynamic polarization parameters of uncoated and coated SS316L in a 1 M H_2SO_4 solution with either H_2 or O_2 purging.

		β_a (V/dec)	β_c (V/dec)	E_{corr} (V)	i_{corr} ($\mu A\,cm^{-2}$)	R_p ($\Omega\,cm^2$)
SS316L	H_2	0.075	0.093	−0.27	20.2	893.63
	O_2	0.048	0.064	−0.24	1.90	6276.56
TiN	H_2	0.14	0.11	−0.38	4.07	6580.49
	O_2	0.057	0.036	−0.34	31.50	304.55
CrN	H_2	0.011	0.0096	−0.32	1.41	1580.70
	O_2	0.021	0.025	−0.34	1.31	3787.93
TiAlN	H_2	0.027	0.032	−0.36	317.00	20.09
	O_2	0.018	0.020	−0.36	18.6	221.45

Note: β_a, β_c, E_{corr}, i_{corr}, and R_p are the Tafel slopes of the anodic and cathodic reactions, the corrosion potential, corrosion current density and polarization resistance, respectively.

the SS316L is in the passive state. However, since the primary passive potential (E_{pp}) is −0.15 V, which is very close to the anode application potential (E_{ap}), the current density of SS316L at −0.1 V is still very high at 1.53×10^{-4} A cm^{-2}. The E_{pp} in the anodic environment of coatings TiN, CrN and TiAlN are −0.26, −0.23 and −0.17 V, respectively. Thus, at the E_{ap}, the TiN-, CrN- and TiAlN-coated materials are all in a passive state, with corrosion current densities of 1.04×10^{-5}, 2.10×10^{-5}, and 3.96×10^{-2} A cm^{-2}, correspondingly. At the cathodic environment (Fig. 5(b)) and cathodic application potential (E_{cp} = +0.6 V vs. Ag/AgCl electrode), the uncoated and TiN-, CrN-, TiAlN-coated specimens are all in the passive state (Fig. 5(b)) and the current densities are 1.0×10^{-5}, 1.16×10^{-4}, 5.24×10^{-5}, and 1.69×10^{-2} A cm^{-2}, respectively. At the simulated anodic conditions, the current density of CrN is higher than that of TiN but in the same order of magnitude (10^{-5} A cm^{-2}), which is one order of magnitude lower than that of uncoated SS316L. In the simulated cathodic conditions (Fig. 5 (b)), uncoated SS316L has the lowest corrosion current density and the CrN coating has a lower current density than the TiN coating.

The potentiodynamic corrosion tests indicate that R_p values of uncoated and coated SS316L are affected significantly by the O_2 or H_2 environment. The good corrosion protection performance of uncoated SS316L is attributed to a passive Cr-oxide layer on the sample surface and an O_2 environment can accelerate the formation of a thick Cr-oxide layer, thus, SS316L has a higher R_p in an O_2 environment than in H_2 environment. This same reason can also be used to explain the higher R_p in an O_2 environment than in H_2 environment for CrN. However, unlike CrN, the passive film on the TiN coating is an oxynitride (Ti–O–N) compound [44] which gradually dissolved during the corrosion tests. The oxynitride might allow rapid diffusion of oxygen, which could accelerate the oxidization of TiN in the O_2 environment and deteriorate the coating structure. Thus, in the O_2 environment, the TiN-coated material showed a lower corrosion resistance than in a H_2 environment.

3.4. Potentiostatic measurements

Fig. 6(a) and (b) shows the potentiostatic polarization curves at −0.1 V vs. Ag/AgCl electrode in a H_2-purged solution and +0.6 V vs. Ag/AgCl electrode in an O_2-purged solution, respectively. In the anodic environment (Fig. 6(a)), SS316L shows a slight increase in the anodic current density during the first 0.5 h then becomes stable and finally reaches 145 $\mu A\,cm^{-2}$ at the end of the test. At the beginning stages (within the first 19 min), the TiN- and CrN-coated materials show lower polarization current densities than the uncoated stainless steel (Fig. 6(a)) at −0.1 V vs. Ag/AgCl electrode which is consistent with the potentiodynamic polarization curves (Fig. 5(a)). For example, at the 10-min test time, the polarization current densities of TiN, CrN and SS316L are 1.04×10^{-5}, 1.79×10^{-5} and 5.18×10^{-5} A cm^{-2}, respectively. However, after about 35 min test time, the current densities of the TiN- and CrN-coated materials are higher than that of uncoated stainless steel and reach up to 0.01 A cm^{-2} magnitude. TiAlN coating is rapidly corroded in the simulated anode test environment and the corrosion current density increases from the 10^{-4} to the 10^{-2} A cm^{-2} magnitude.

The potentiostatic polarization curves in the simulated cathodic environment, i.e., +0.6 V application potential and oxygen purging, are shown in Fig. 6(b). Compared with the curves for tests in the anodic environment (Fig. 6(a)), the current densities of all the materials in the cathodic environment are much lower. At the early period (about 45 min), the current densities are in the order of SS316L < CrN < TiN < TiAlN which is consistent with the potentiodynamic corrosion test results (Fig. 5(b)). After 45 min test time, the polarization current density of CrN-coated and uncoated SS316L are similar at about 1.1 $\mu A\,cm^{-2}$. The current density of TiN (18.0 $\mu A\,cm^{-2}$) is higher than those of CrN coating and SS316L. The TiAlN coating, in the initial stages, has a similar current density to the TiN coating, whereas the current density gradually increases with time and reaches 0.001 A cm^{-2} at the end of test, which is two and three orders of magnitude higher than that of the CrN and TiN coatings.

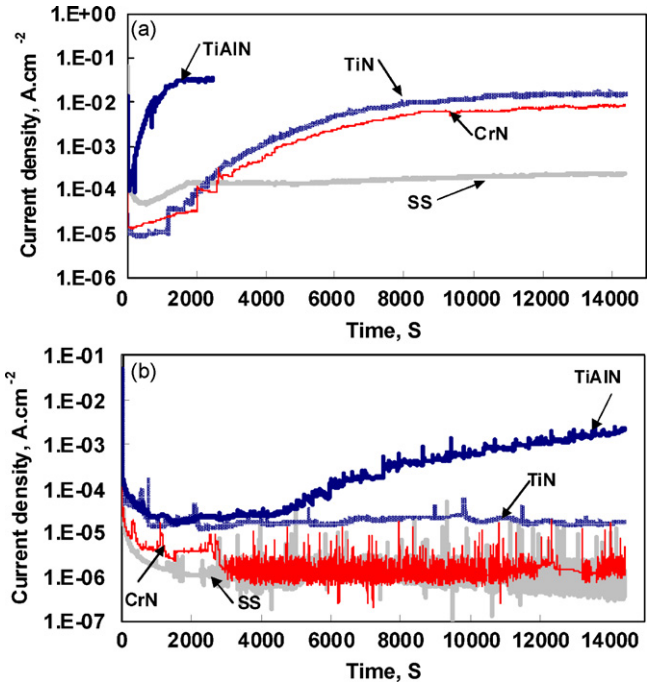

Fig. 6. Potentiostatic polarization behaviors of TiN-, CrN-, TiAlN-coated and uncoated stainless steel 316L at (a) −0.1 V vs. Ag/AgCl reference electrode with H_2 purging and (b) +0.6 V vs. Ag/AgCl reference electrode with O_2 purging in a 1 M sulphuric acid solution at 70 °C for 4 h.

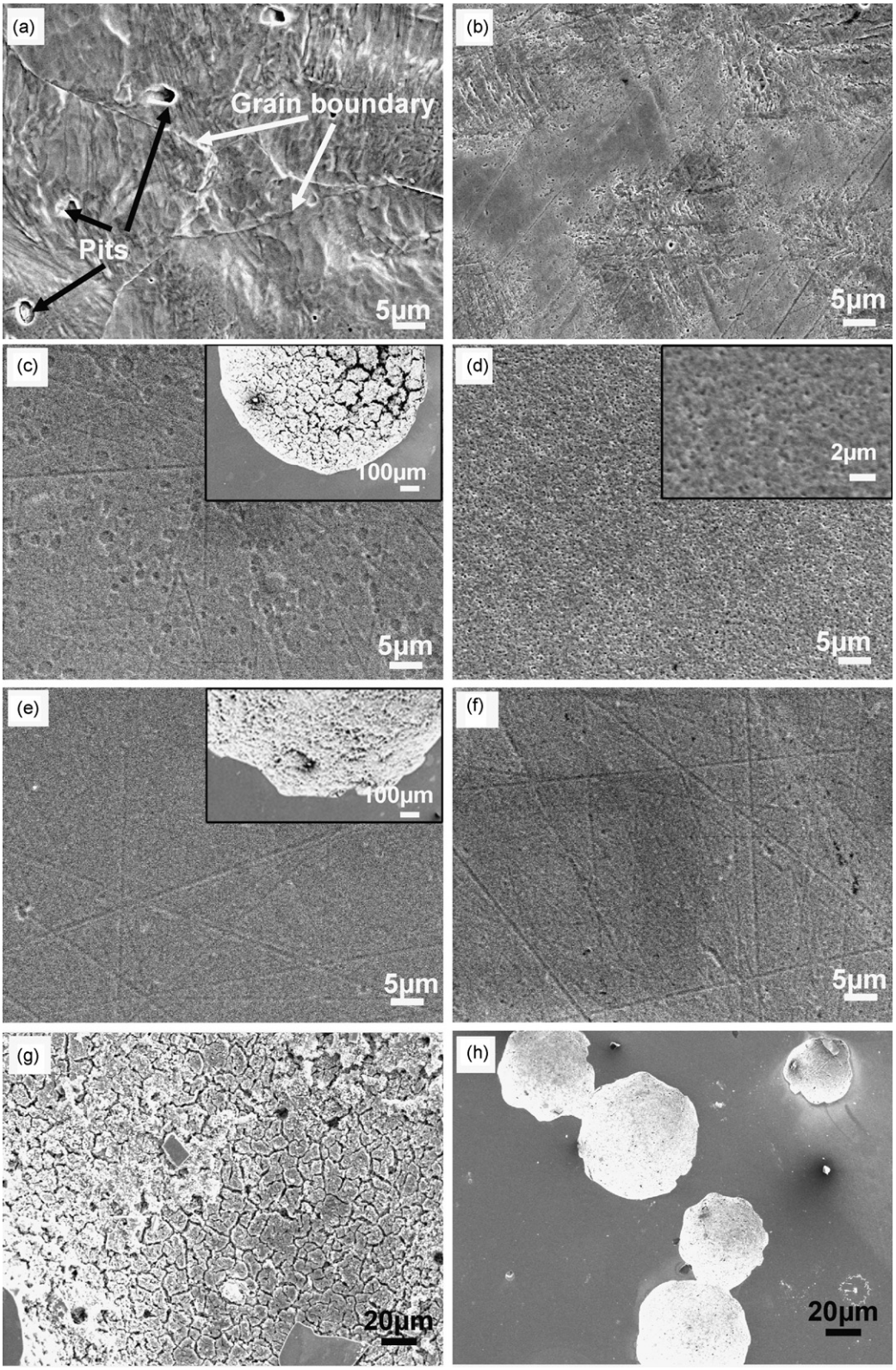

Fig. 7. SEM micrographs of (a and b) uncoated, (c and d) TiN-, (e and f) CrN- and (g and h) TiAlN-coated stainless steel 316L after potentiostatic polarization corrosion test in the simulated (a, c, e, and g) anodic and (b, d, f, and h) cathodic environments. The insets in (c) and (e) are the low magnification images of surfaces to show one pitting hole on the corresponding surface and the inset in (d) is the magnified image of (d) to show the corroded surface.

Fig. 7(a and b) shows the SEM micrographs of the surface of uncoated stainless steel after potentiostatic polarization testing in the anodic and cathodic conditions, respectively. In the anodic environment (Fig. 7(a)), pits and etched grain boundaries can be clearly observed. After testing in the cathodic environment (Fig. 7(b)), corrosion occurs not only at the grain boundaries but also all over the surface and some brown corrosion products are present. For both the TiN and CrN coatings after potentiostatic polarization test-

ing in the anodic environment (Fig. 7(c and e) respectively), there was a large pit in the corroded area though no corrosion or corrosion deposits was observed at the other regions of the corrosion test area. These observations imply that in the anodic conditions, the corrosion initiated at some specific location, such as a pinhole in the coating structure, which were formed during the PVD deposition processes. Around the initial corrosion spot, the coating cracked and spalled off due to the adhesion failure along the coating/substrate interface. With an increase in exposure time, a large pit gradually formed. For the TiN and CrN coatings in the cathodic environment (Fig. 7(d and f)), no pits or corrosion deposits were observed but general overall corrosion had taken place (the inset in Fig. 7(d)). Thus, the TiN and CrN coatings can protect the stainless steel from corrosion at the anode application potential since the corrosion current density of the coatings is lower than that of the uncoated stainless steel as shown in both the potentiodynamic polarization test (Fig. 5(a)) and at the early stages of the potentiostatic corrosion tests (Fig. 6(a)). However, any pinholes existing in the corrosion test area of TiN and CrN coatings can provide a site for enhanced local corrosion. After some period of testing, the stainless steel substrate began to corrode at the pinhole site. Based on the potentiodynamic polarization corrosion curves (Fig. 5(a)), the stainless steel substrate exhibited a higher current density than the TiN- and CrN-coated materials in the anodic environment (anode application voltage: −0.1 V vs. reference electrode in H_2 bubbled environment). Thus, in the anodic environment, accelerated and localized corrosion would occur at pinhole sites due to the small exposed surface area of the stainless steel substrate within the pinholes. However, in the cathodic environment (cathode application voltage: +0.6 V vs. reference electrode in O_2 bubbled environment), the substrate stainless steel had a lower corrosion current density than the TiN and CrN coatings based on the potentiodynamic polarization corrosion tests at simulated cathodic conditions (Fig. 5 (b)). The large surface areas of the coatings, which have less corrosion resistance than stainless steel in the cathodic environment, would exhibit general corrosion instead of the localized corrosion. Thus, at the cathodic conditions, the negative effect of pinholes in the coatings on the corrosion resistance is minor. Moreover, the cathodic environment also provided a better passivation ability compared with the anodic environment. Since a passive Cr-oxide layer on the CrN coating is believed denser than a passive Ti oxide layer on the TiN coating [45], the CrN coating is superior to the TiN coatings in both anodic and cathodic environments.

Fig. 7(g and h) shows that the TiAlN coating has the worst corrosion resistance under the potentiostatic test conditions. In the simulated anodic conditions (Fig. 7(g)), after about 40 min potentiostatic testing, the current density reaches 0.1 A cm^{-2} and the TiAlN coating almost disappeared and the stainless steel substrate was exposed. In the cathodic conditions (Fig. 7(h)) after 4 h potentiostatic testing, several large pits could be observed even by the naked eye.

The TiAlN coating exhibited the poorest corrosion properties in the simulated PEM fuel cell conditions in both the potentiodynamic and potentiostatic polarization corrosion tests. The poorer corrosion resistance of TiAlN compared to TiN in acid solution has also been reported by Li et al. [33]. At the TiAlN coating surface, a Ti–Al–O layer exists naturally, and this layer may readily be dissolved in a sulphuric acid solution. Therefore, unlike the situation for cutting tool applications, where the TiAlN coating has a higher hardness and improved high temperature oxidation resistance compared to a TiN coating, the partial replacement of Ti with Al in the cubic TiN structure likely degrades the corrosion resistance of the coating in the simulated PEMFC conditions. The inferior corrosion property may be due to the fact that the chemical composition of the TiAlN coating in this study is Ti:Al:N = 35:15:50 (at.%) and no the AlN phase exists in the coating. However, a TiAlN coating with different chemical composition and phase structure could exhibit different electrochemical behavior.

Compared with the stainless steel 316L, the CrN-coated material has a better corrosion resistance in the anode environment based on potentiodynamic polarization corrosion tests and a similar corrosion resistance in the cathodic environment as shown in potentiostatic corrosion tests. Given that the contact resistance of the CrN-coated SS316L is significantly lower than that of the uncoated SS316L reference material, the PVD CrN-coated SS316L could be used as an alternative bipolar plate material which would have both a low contact resistance and high corrosion resistance.

Generally speaking, this study provided a better understanding of PVD coatings performance in simulated anodic and cathodic environments of PEMFCs and, as a result, some new directions for future research on PVD coatings can be suggested. As well as developing new coating materials, eliminating pinholes will be among the most critical tasks, particularly for coatings applied to the anodic bipolar plates. EBPVD is usually considered as a better coating deposition process than either magnetron sputtering or cathodic arc PVD in terms of coating smoothness and density. Fewer pinholes are also produced in EBPVD coatings, compared to the coatings prepared by magnetron sputtering and cathodic arc deposition processes [46]. More attention should be paid to the cleanliness of the substrates before coating and the contamination in the vacuum chamber to help avoid pinhole formation. An interrupted coating process, or multilayered coatings, may “disconnect” the pinholes and prevent through-coating pinholes. A CrN/TiN multilayered coating may be able to synergistically combine their advantages (i.e., TiN is better as an anode and CrN is better as a cathode material) for a universal coating that has superior performance as both anodic and cathodic electrodes.

4. Conclusions

Both the EBPVD TiN based (TiN and TiAlN) coatings exhibit a NaCl-typed phase structure. The CrN coating has an orthorhombic CrN crystal structure with an amount of the β-Cr_2N phase. Although the TiN coating had the highest elastic modulus, the TiAlN coating had the highest hardness among those three coatings. The order of the contact resistance (CR) is TiAlN < CrN < TiN < SS316L.

The potentiodynamic polarization corrosion test results showed that the O_2 and H_2 environments significantly affected the polarization characteristics of all coatings and uncoated SS316L. The SS316L, CrN- and TiAlN-coated samples have a higher corrosion resistance in the cathodic environment (with O_2 purging) than in the anodic environment (with H_2 purging). On the other hand, the TiN coating has a higher corrosion resistance in the anodic environment than in the cathodic environment. The ranking for corrosion resistance in H_2 or O_2 bubbled environments was TiN > CrN > SS316L > TiAlN and SS316L > CrN > TiN > TiAlN, respectively, based on the potentiodynamic polarization corrosion tests.

The potentiostatic corrosion tests show that in the simulated anodic conditions (−0.1 V vs. Ag/AgCl electrode), both TiN and CrN have a lower corrosion current density than SS316L, but with increasing test time, the current density increases because corrosion has been initiated at pinholes in the coatings. In the simulated cathodic conditions, since the SS316L substrate at the pinhole sites can be readily passivated, and thus provide higher corrosion protection, the negative effect of pinholes in the coatings is minor. TiN has a higher corrosion current density than SS316L in the cathodic test conditions, whereas, the CrN coating shows a similar value to SS316L. The electrochemical test results indicate that the TiAlN coating prepared in this work has the poorest corrosion resistance in environments simulating operations in PEM fuel cells.

Since the EBPVD CrN coating has a low contact resistance and high (in the anodic environment) or similar (in the cathodic envi-

ronment) corrosion resistance, compared with the SS316L, the CrN-coated material can be used as an alternative bipolar plate material. The EBPVD process greatly reduced number of pinholes existing in the coatings compared to other PVD processes but more research work is required to help eliminate pinholes for the long-term durability of such coatings for PEM fuel cell applications.

Acknowledgements

This research was supported by the Natural Science and Engineering Research Council of Canada (NSERC). L. Wang would also like to acknowledge NSERC for the award of a Canada Graduate Scholarship.

References

[1] V. Mehta, J.S. Cooper, Journal of Power Sources 114 (2003) 32–53.
[2] C.Y. Wang, Chemical Reviews 104 (2004) 4727–4765.
[3] J. Wind, R. Spah, W. Kaiser, G. Bohm, Journal of Power Sources 105 (2002) 256–260.
[4] A.J. Appleby, Energy 21 (1996) 521–653.
[5] A. Hermann, T. Chaudhuri, P. Spagnol, International Journal of Hydrogen Energy 30 (2005) 1297–1302.
[6] H. Tawfik, Y. Hung, D. Mahajan, Journal of Power Sources 163 (2007) 755–767.
[7] Y.Y. Shao, G.P. Yin, Z.B. Wang, Y.Z. Gao, Journal of Power Sources 167 (2007) 235–242.
[8] N.D.L. Heras, E.P.L. Roberts, R. Langton, D.R. Hodgson, Energy & Environmental Science 2 (2009) 206–214.
[9] H.L. Wang, M.A. Sweikart, J.A. Turner, Journal of Power Sources 115 (2003) 243–251.
[10] S.J. Lee, C.H. Huang, Y.P. Chen, Journal of Materials Processing Technology 140 (2003) 688–693.
[11] S.J. Lee, C.H. Huang, Y.P. Chen, C.T. Hsu, Journal of Fuel Cell Science and Technology 2 (2005) 290–294.
[12] B. Cunningham, D.G. Baird, Journal of Materials Chemistry 16 (2006) 4385–4388.
[13] H.L. Wang, J.A. Turner, Journal of Power Sources 180 (2008) 791–796.
[14] R.J. Tian, J.C. Sun, J.L. Wang, International Journal of Hydrogen Energy 33 (2008) 7507–7512.
[15] Y. Wang, D.O. Northwood, Advanced Materials Research 41–42 (2008) 469–475.
[16] Y. Wang, O. Northwood, Electrochimica Acta 52 (2007) 6793–6798.
[17] T. Fukutsuka, T. Yamaguchi, S.I. Miyano, Y. Matsuo, Y. Sugie, Z. Ogumi, Journal of Power Sources 174 (2007) 199–205.
[18] Y. Show, Surface & Coatings Technology 202 (2007) 1252–1255.
[19] M.C. Li, S.Z. Luo, C.L. Zeng, J.N. Shen, H.C. Lin, C.N. Cao, Corrosion Science 46 (2004) 1369–1380.
[20] Y. Wang, D.O. Northwood, International Journal of Hydrogen Energy 32 (2007) 895–902.
[21] Y. Wang, D.O. Northwood, Journal of Power Sources 165 (2007) 293–298.
[22] E.A. Cho, U.S. Jeon, S.A. Hong, I.H. Oh, S.G. Kang, Journal of Power Sources 142 (2005) 177–183.
[23] L. Wang, X. Nie, J. Housden, E. Spain, J.C. Jiang, E.I. Meletis, A. Leyland, A. Matthews, Surface & Coatings Technology 203 (2008) 816–821.
[24] P. Zhang, L. Wang, X. Nie, Surface & Coatings Technology 201 (2007) 5176–5181.
[25] V.K.W. Grips, H.C. Barshilia, V.E. Selvi, Kalavati, K.S. Rajam, Thin Solid Films 514 (2006) 204–211.
[26] T. Polcar, T. Kubart, R. Novak, L. Kopecky, P. Siroky, Surface & Coatings Technology 193 (2005) 192–199.
[27] Y.H. Yoo, D.P. Le, J.G. Kim, S.K. Kim, P. Van Vinh, Thin Solid Films 516 (2008) 3544–3548.
[28] A. Conde, C. Navas, A.B. Cristobal, J. Housden, J. de Damborenea, Surface & Coatings Technology 201 (2006) 2690–2695.
[29] M. BinSudin, A. Leyland, A.S. James, A. Matthews, J. Housden, B. Garside, Surface & Coatings Technology 81 (1996) 215–224.
[30] S.Y. Kim, D.H. Han, J.N. Kim, J.J. Lee, Journal of Power Sources 193 (2009) 570–574.
[31] H.S. Choi, D.H. Han, W.H. Hong, J.J. Lee, Journal of Power Sources 189 (2009) 966–971.
[32] N.D. Nam, J.G. Kim, Japanese Journal of Applied Physics 47 (2008) 6887–6890.
[33] Y. Li, L. Qu, F.H. Wang, Corrosion Science 45 (2003) 1367–1381.
[34] X.B. Liu, C. Johnson, C.M. Li, J. Xu, C. Cross, International Journal of Hydrogen Energy 33 (2008) 189–196.
[35] E. Spain, J.C. Avelar-Batista, M. Letch, J. Housden, B. Lerga, Surface & Coatings Technology 200 (2005) 1507–1513.
[36] W.C. Oliver, G.M. Pharr, Journal of Materials Research 7 (1992) 1564–1583.
[37] Y.H. Cheng, B.K. Tay, S.P. Lau, Journal of Vacuum Science & Technology B 20 (2002) 2000–2006.
[38] L.M. Liu, S.Q. Wang, H.Q. Ye, Acta Materialia 52 (2004) 3681–3688.
[39] A.A. Irudayaraj, P. Kuppusami, S. Kalainathan, Surface Engineering 24 (2008) 28–35.
[40] E. Martinez, R. Sanjines, O. Banakh, F. Levy, Thin Solid Films 447–448 (2004) 332–336.
[41] M.P. Brady, K. Weisbrod, C. Zawodzinski, I. Paulauskas, R.A. Buchanan, L.R. Walker, Electrochemical and Solid-State Letters 5 (2002) A245–A247.
[42] M.P. Brady, K. Weisbrod, I. Paulauskas, R.A. Buchanan, K.L. More, H. Wang, M. Wilson, F. Garzon, L.R. Walker, Scripta Materialia 50 (2004) 1017–1022.
[43] B. Yang, M.P. Brady, H. Wang, J.A. Turner, K.L. More, D.J. Young, P.F. Tortorelli, E.A. Payzant, L.R. Walker, Journal of Power Sources 174 (2007) 228–236.
[44] F. Esaka, K. Furuya, H. Shimada, M. Imamura, N. Matsubayashi, H. Sato, A. Nishijima, A. Kawana, H. Ichimura, T. Kikuchi, Journal of Vacuum Science & Technology a-Vacuum Surfaces and Films 15 (1997) 2521–2528.
[45] S. Rudenja, C. Leygraf, J. Pan, P. Kulu, E. Talimets, V. Mikli, Surface and Coatings Technology 114 (1999) 129–136.
[46] S. PalDey, S.C. Deevi, Materials Science and Engineering A 342 (2003) 58–79.